GEOPHYSICS, VOL. 82, NO. 2 (MARCH-APRIL 2017); P. S99–S109, 13 FIGS.
10.1190/GEO2015-0167.1

Converted-wave seismic imaging: Amplitude-balancing source-independent imaging conditions

Andrey H. Shabelansky[1], Alison Malcolm[2], and Michael Fehler[3]

ABSTRACT

We have developed crosscorrelational and deconvolutional forms of a source-independent converted-wave imaging condition (SICW-IC) and show the relationship between them using a concept of conversion ratio coefficient, a concept that we developed through reflection, transmission, and conversion coefficients. We applied the SICW-ICs to a two half-space model and the synthetic Marmousi I and II models and show the sensitivity of the SICW-ICs to incorrect wave speed models. We also compare the SICW-ICs and source-dependent elastic reverse time migration. The results of SICW-ICs highlight the improvements in spatial resolution and amplitude balancing with the deconvolutional forms. This is an attractive alternative to active and passive source elastic imaging.

INTRODUCTION

Seismic imaging of the earth's interior is important in exploration and global seismology. It produces images of subsurface discontinuities associated with impedance contrasts through reflection, transmission, or conversion coefficients of propagating waves. One of the pioneering studies on seismic imaging is presented by Claerbout (1971) who introduces the concept of a reflective imaging condition (IC). This concept is based on the fundamental assumption that the acquisition/survey geometry is well-known: The source and receiver locations are known, and seismic waves can be numerically propagated from these locations. This imaging condition has been extensively investigated for the past five decades with algorithms for post and prestack migrations, such as the survey sinking migration (Claerbout, 1985; Popovici, 1996), Kirchhoff-type migration (Schneider, 1978; Bleistein, 1987), shot profile migration (Stoffa et al., 1990), and reverse time migration (Baysal et al., 1983; Chang and McMechan, 1994). However, when source information is not available, seismic images cannot be constructed using Claerbout's approach. An alternative approach is to use interference between different wave types propagated backward in time from receiver locations only (Nihei et al., 2001; Xiao and Leaney, 2010; Brytic et al., 2012; Shang et al., 2012; Shabelansky et al., 2013a, 2014). We call this imaging condition the source-independent converted-wave imaging condition (SICW-IC). We discuss the physical meaning of the SICW-IC and present an amplitude-balancing approach for SICW imaging.

This paper is divided into three parts. In the first part, we review the relationship between Claerbout (1971) and SICW-ICs with reflection, transmission, and conversion coefficients. In the second part, we introduce the concept of conversion ratio coefficients (CRCs) and we show how to associate them with different forms of SICW-IC. In the final part, we present numerical tests of different forms of SICW-IC applied to a two half-space model and the synthetic Marmousi I and II models. We also show the sensitivity of the SICW-ICs to wave speed variations and present a comparison between the SICW-ICs and source-dependent elastic reverse time migration (RTM).

RELATIONSHIP BETWEEN IMAGING CONDITIONS AND REFLECTION, TRANSMISSION, AND CONVERSION COEFFICIENTS

In this section, we present four forms of a source-independent converted-wave imaging condition following the approach of Claerbout (1971) for the standard imaging condition.

First presented at the EAGE 2015 Annual Meeting (Shabelansky et al., 2015a).
Manuscript received by the Editor 10 March 2015; revised manuscript received 18 October 2016; published online 7 February 2017.
[1]Formerly Massachusetts Institute of Technology, Department of Earth, Atmospheric and Planetary Sciences, Earth Resources Laboratory, Cambridge, Massachusetts, USA; presently Chevron, Houston, Texas, USA. E-mail: andreys@alum.mit.edu.
[2]Formerly Massachusetts Institute of Technology, Department of Earth, Atmospheric and Planetary Sciences, Earth Resources Laboratory, Cambridge, Massachusetts, USA; presently Memorial University of Newfoundland, Earth Sciences Department, Newfoundland, Canada. E-mail: amalcolm@mun.ca.
[3]Massachusetts Institute of Technology, Department of Earth, Atmospheric and Planetary Sciences, Earth Resources Laboratory, Cambridge, Massachusetts, USA. E-mail: fehler@mit.edu.

Standard imaging condition

The relationship between the reflection (or reflection conversion) coefficients R associated with impedance contrasts (see Figure 1a), is defined as the ratio between the pure reflected (or reflected converted) and the incident wavefields u:

$$R_{PP} = \frac{u^r_{PP}}{u^i_P}, \qquad R_{PS} = \frac{u^r_{PS}}{u^i_P}, \tag{1}$$

and for the transmission (or transmission conversion) coefficients T as the ratio between the pure transmitted (or transmitted converted) and the incident wavefields:

$$T_{PP} = \frac{u^t_{PP}}{u^i_P}, \qquad T_{PS} = \frac{u^t_{PS}}{u^i_P}. \tag{2}$$

For simplicity we omit the vector notation of the wavefield u (e.g., displacement, particle velocity, or acceleration) and the spatial and time indices. Superscripts i, r, and t refer to the incident, reflected, and transmitted waves, respectively, and subscripts P and S denote the wave type, P and/or S. The wavefields u^r_{PS} and u^t_{PS} are called the P to S reflected converted and transmitted converted, respectively.

The imaging condition in Claerbout (1971) approximates R_{PP}, where the incident wavefield is calculated by forward propagation in time from the source and is often called the source wavefield, and the reflected (or reflected-converted) wavefield is calculated by back propagation in time from the receivers and is called the receiver wavefield. The incident wavefield in the denominator of equations 1 and 2 can be zero. Many studies have investigated how to avoid the division by zero and suggest different solutions (Valenciano and Biondi, 2003; Kaelin and Guitton, 2006; Chattopadhyay and McMechan, 2008; Schleicher et al., 2008). One solution is to multiply the numerator and denominator by the denominator and to add a small number to the denominator (Valenciano and Biondi, 2003). Thus, for equation 1, we obtain

$$I^D_{PP} = \frac{u^i_P u^r_{PP}}{(u^i_P)^2 + \epsilon^2}, \qquad I^D_{PS} = \frac{u^i_P u^r_{PS}}{(u^i_P)^2 + \epsilon^2}, \tag{3}$$

where I is the calculated image and ϵ^2 is a small number. This form is called a deconvolutional imaging condition, denoted with the superscript D. The results obtained with this imaging condition depend strongly on the choice of ϵ^2, which changes with the data due to illumination and noise, and the image may still be unstable. As an alternative to the deconvolutional imaging condition, Claerbout (1971) also introduces the crosscorrelational imaging condition by taking only the numerator of equation 3 giving

$$I^C_{PP} = u^i_P u^r_{PP}, \qquad I^C_{PS} = u^i_P u^r_{PS}, \tag{4}$$

where the superscript C refers to crosscorrelation. Unlike the deconvolutional imaging condition that has no units just like the reflection and transmission (or reflection conversion and transmission conversion) coefficients, the crosscorrelational imaging condition has the squared units of the wavefields that form the image. Figure 1b shows schematically the application of the concept of the imaging condition between forward-propagating (incident) P and backward-propagating (reflected) P wavefields, and in Figure 1c between forward-propagating (incident) P and backward-propagating (reflected-converted) S wavefields. Note that with Claerbout (1971) imaging condition, only one reflected or reflected-converted wavefield (i.e., either PP or PS) is used at a time during the propagation and the other wave type, marked with the gray line, is not used.

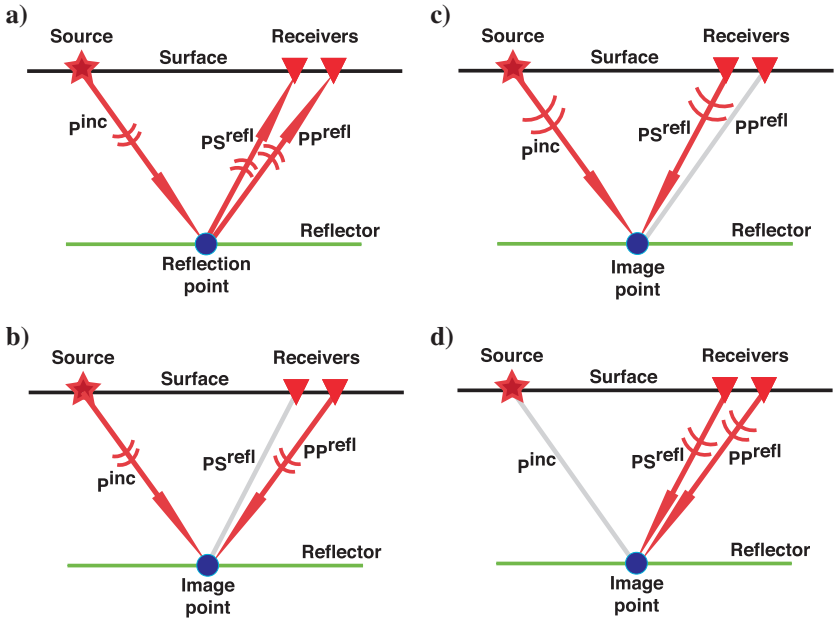

Figure 1. Schematics illustrating (a) elastic-wave propagation that samples a point (blue dot) on a reflector with an incident P-wave, (b) imaging of the reflection point using Claerbout's imaging condition with forward- and backward-propagating P-waves, and with (c) forward-propagating P-wave and backward-propagating S-wave. (d) SICW-IC with P and S backward-propagating waves. The red arrows in panels (b-d) indicate the direction of the propagating waves that form an image. The gray lines mark the available wave types that are not used in the image construction. Although the source information, marked with a star, indicates the origin of the waves, the image obtained with SICW-IC in panel (d) uses receiver information only.

Source-independent converted-wave imaging condition

The source-independent converted-wave imaging condition uses both back-propagated wavefields simultaneously (see Figure 1d) in the crosscorrelational form as

$$I^C = u^r_{PP} u^r_{PS}. \tag{5}$$

The source location, marked with the star in Figure 1d, is not used for the SICW-IC because we use only the reflected and reflected-converted wavefields (i.e., the incident wavefield marked with the gray line is not used). Moreover, the source location can be anywhere along the gray lines in Figure 2, which makes SICW-IC applicable to active and passive seismic data. The sources along these gray lines can, in general, be outside of the computational grid and the image is constructed only in

the vicinity of the receivers (i.e., far from the sources). Not only is the source location not used in the process, but no other source information (e.g., mechanism and time function) is required to form the SICW image. However, because the recorded seismic signal depends on the source that generated the seismic waves and the path along which they travel and interfere with subsurface, the quality of the SICW image will be dependent on the source information characteristics. The SICW-IC is also computationally efficient because it uses only one elastic-wave propagation, backward in time, during which the back-propagated (either displacement or particle velocity) vector wavefield is simultaneously separated into the P- and S-wavefield components and the image is formed (using SICW-IC) without storing (and subsequently reading) any of the separated wavefields, as is common practice for (acoustic and elastic) standard RTM. The separation approach is given in detail in Appendix A.

As reviewed above, Claerbout's imaging condition is directly related to reflection and reflection-conversion coefficients. However, SICW-IC is instead associated with the relative energy between pure reflected (or transmitted) and the converted reflected (or converted transmitted) waves. To understand what is imaged using this imaging condition, we define the CRC as the ratio between the reflection or transmission coefficients of the converted and pure wave modes. For an incident P-wave, this gives

$$\mathrm{CRC}^r = \frac{R_{\mathrm{PS}}}{R_{\mathrm{PP}}} = \frac{\frac{u^r_{\mathrm{PS}}}{u^i_{\mathrm{P}}}}{\frac{u^r_{\mathrm{PP}}}{u^i_{\mathrm{P}}}} = \frac{u^r_{\mathrm{PS}}}{u^r_{\mathrm{PP}}} \tag{6}$$

and

$$\mathrm{CRC}^t = \frac{T_{\mathrm{PS}}}{T_{\mathrm{PP}}} = \frac{\frac{u^t_{\mathrm{PS}}}{u^i_{\mathrm{P}}}}{\frac{u^t_{\mathrm{PP}}}{u^i_{\mathrm{P}}}} = \frac{u^t_{\mathrm{PS}}}{u^t_{\mathrm{PP}}}, \tag{7}$$

where the superscripts r and t denote the reflected and transmitted wavefields, respectively. The obtained CRCs define the ratio between the converted and pure seismic waves and how their energy is partitioned after passing through an impedance contrast. Although the CRC is independent of the incident wavefield, it does depend on the angle of incidence, which can be tracked using Snell's law through reflected and reflected-converted (and/or transmitted and transmitted converted) angles. The CRCs can be similarly defined for an incident S-wave.

From equations 6 and 7, we define the source-independent converted-wave imaging condition similarly to Claerbout's deconvolutional IC as

$$I^r_{\mathrm{PS}} = \frac{u^r_{\mathrm{PP}} u^r_{\mathrm{PS}}}{(u^r_{\mathrm{PP}})^2 + \epsilon^2}, \qquad I^t_{\mathrm{PS}} = \frac{u^t_{\mathrm{PP}} u^t_{\mathrm{PS}}}{(u^t_{\mathrm{PP}})^2 + \epsilon^2}. \tag{8}$$

When we back-propagate entire seismic records, even though we separate (during the reverse time propagation) the total wavefield into the P- and S-wavefields, we do not distinguish between reflected, transmitted, and converted waves and their modes of incidence. We, therefore, omit the superscript and the first subscript letter of the wavefield u in equation 8 (i.e., we write P instead of PP and S instead of PS). Thus, an explicit form of the deconvolutional SICW-IC for each term of equation 8, integrated over time and summed over N_{S} sources, for an incident P-wave is

$$I^D_{\mathrm{P}}(\mathbf{x}) = \sum_j^{N_{\mathrm{S}}} \int_T^0 \frac{\mathbf{u}^j_{\mathrm{P}}(\mathbf{x},t) \cdot \mathbf{u}^j_{\mathrm{S}}(\mathbf{x},t)}{(\mathbf{u}^j_{\mathrm{P}}(\mathbf{x},t))^2 + \epsilon^2} dt, \tag{9}$$

and that for incident S-wave is

$$I^D_{\mathrm{S}}(\mathbf{x}) = \sum_j^{N_{\mathrm{S}}} \int_T^0 \frac{\mathbf{u}^j_{\mathrm{S}}(\mathbf{x},t) \cdot \mathbf{u}^j_{\mathrm{P}}(\mathbf{x},t)}{(\mathbf{u}^j_{\mathrm{S}}(\mathbf{x},t))^2 + \epsilon^2} dt, \tag{10}$$

where the lowercased bold letter denotes a vector and $\cdot$ is the dot product between two vector wavefields. The subscript of I denotes the wavefield of the denominator, which we call the illuminating wavefield. The time and spatial coordinates are t and $\mathbf{x} = (x, y, z)$ in 3D (or (x, z) in 2D), and the (new) superscript j is the source index. The ICs in equations 9 and 10 construct images only from combinations between the pure and the converted-wave modes because the pure wave modes (PP and SS) are separated in time during the back-propagation and their combination should not contribute to the image. The same holds true for the combination between PS and SP. Equivalent forms of the ICs in equations 9 and 10 can be derived in the frequency domain as in Claerbout (1985).

By taking the numerator only, we obtain an explicit crosscorrelational SICW-IC form (Shabelansky et al., 2014):

$$I^C(\mathbf{x}) = \sum_j^{N_{\mathrm{S}}} \int_T^0 \mathbf{u}^j_{\mathrm{P}}(\mathbf{x},t) \cdot \mathbf{u}^j_{\mathrm{S}}(\mathbf{x},t) dt. \tag{11}$$

The crosscorrelational SICW-IC is unconditionally stable. However, because the denominator is omitted, the crosscorrelational image is not amplitude balanced.

To investigate how we might obtain an amplitude balanced IC, we evaluate the CRCs and their relationship with SICW-IC using an

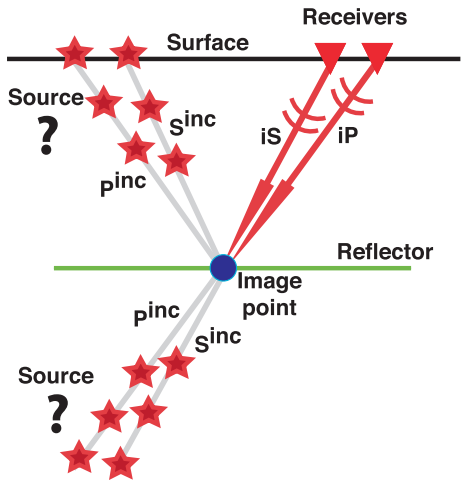

Figure 2. A schematic showing a generalization of SICW-IC for reflection and transmission seismic data with either (or both) incident P- or/and S-wavefield(s). The red arrows indicate the direction in which the recorded wavefields are back-propagated to form an image. The gray lines mark available wave types that are not used in the image construction. The index i marks an incident wave, and it can be either P or S. Although source information, marked with stars, indicates the origin of the waves, the image obtained with SICW-IC uses the receiver information only.

example of a two half-space model from Aki and Richards (2002, p. 148) with P- and S-wave speeds $V_P = 4$ km/s and $V_S = 2$ km/s, respectively, density $\rho = 2$ kg/m^3 and contrasts $\Delta V_P = 0.5$ km/s, $\Delta V_S = 0.1$ km/s, and $\Delta\rho = 0.1$ kg/km^3. We plot the reflection, reflection conversion, transmission, and transmission-conversion coefficients along with their CRCs for an incident P-wave in Figure 3. In Figure 3a, we observe that the CRC is completely uncorrelated with the reflection or reflection-conversion coefficients. For the transmission case (Figure 3b and 3c) because the pure transmitted mode is close to unity, the CRC has good correlation with the transmission-conversion coefficients. More details of this analysis including that for an incident S-waves can found in Shabelansky (2015, chapter 2).

The CRCs presented in equations 6 and 7 and their deconvolutional IC forms, equations 9 and 10, go to infinity when the coefficient or the wavefield in the denominator goes to zero. This contradicts the idea behind an imaging condition: When one wavefield is zero, the image should be zero. Another downside of the imaging condition in equations 9 and 10 is that only one wavefield is used for normalization/illumination (either the P- or S-wave but not both). To alleviate these two limitations while still preserving approximately the CRCs, we propose normalized CRCs (NCRCs), which are given as

$$\mathrm{NCRC}^r = \frac{4R_{\mathrm{PP}}R_{\mathrm{PS}}}{(|R_{\mathrm{PP}}| + |R_{\mathrm{PS}}|)^2} = \frac{4u^r_{\mathrm{PP}}u^r_{\mathrm{PS}}}{(u^r_{\mathrm{PP}})^2 + 2|u^r_{\mathrm{PP}}u^r_{\mathrm{PS}}| + (u^r_{\mathrm{PS}})^2} \tag{12}$$

$$\mathrm{NCRC}^t = \frac{4T_{\mathrm{PP}}T_{\mathrm{PS}}}{(|T_{\mathrm{PP}}| + |T_{\mathrm{PS}}|)^2} = \frac{4u^t_{\mathrm{PP}}u^t_{\mathrm{PS}}}{(u^t_{\mathrm{PP}})^2 + 2|u^t_{\mathrm{PP}}u^t_{\mathrm{PS}}| + (u^t_{\mathrm{PS}})^2}. \tag{13}$$

The NCRCs are zero when one of the waves is zero and are between -1 and 1: The binomial expansion in the denominator and the factor four in the numerator set the values to ± 1 when both wavefields are equal in amplitude with the same or opposite sign. In Figure 4, we show the coefficients calculated using equations 12 and 13 for the two half-space example discussed above. We observe that their behavior is stable.

For imaging purposes, we back-propagate entire seismic records simultaneously without discriminating between reflected and transmitted waves and drop their mode of incidence as in equations 9–11. Thus, the explicit form for the normalized SICW-IC is

$$I^D_{\mathrm{PS}}(\mathbf{x}) = \sum_j^{N_S} \int_T^0 \frac{4\mathbf{u}^j_{\mathrm{P}}(\mathbf{x},t)\cdot\mathbf{u}^j_{\mathrm{S}}(\mathbf{x},t)}{(\mathbf{u}^j_{\mathrm{P}}(\mathbf{x},t))^2 + 2|\mathbf{u}_{\mathrm{P}}(\mathbf{x},t)\cdot\mathbf{u}^j_{\mathrm{S}}(\mathbf{x},t)| + (\mathbf{u}^j_{\mathrm{S}}(\mathbf{x},t))^2 + \epsilon^2} dt, \tag{14}$$

where the subscript of I indicates that we use the P- and S-illuminating wavefields to form an image. We have also added a stabilization factor ϵ^2 to the denominator as in equations 9 and 10. In the next sections, we will investigate numerically each SICW-IC presented in equations 9, 10, 11, and 14, and we highlight the advantages of the normalized SICW-IC. Although we found that setting the ϵ to be between 5% and 10% of the maximum amplitude of the crosscorrelation SICW image with a single source stabilized all forms of the deconvolutional SICW-IC, a better way of estimating the ϵ may be beneficial.

NUMERICAL TESTS

To verify the CRCs from equations 6 and 7 and to examine the stability and illustrate advantages of different forms of the imaging condition, given in equations 9, 10, 11, and 14, we test them with a two half-space model, and the Marmousi I and II synthetic models. We show all imaging results after applying a Laplacian filter (Youn and Zhou, 2001; Zhang and Sun, 2008) to suppress low-frequency artifacts and to enhance the spatial resolution of the images. All elastic-wave solutions for imaging are modeled with a 2D finite-difference solver, using a second order in time staggered-grid spatial-pseudospectral method with perfectly matched layer (PML) absorbing boundary conditions (Shabelansky, 2015, appendix A).

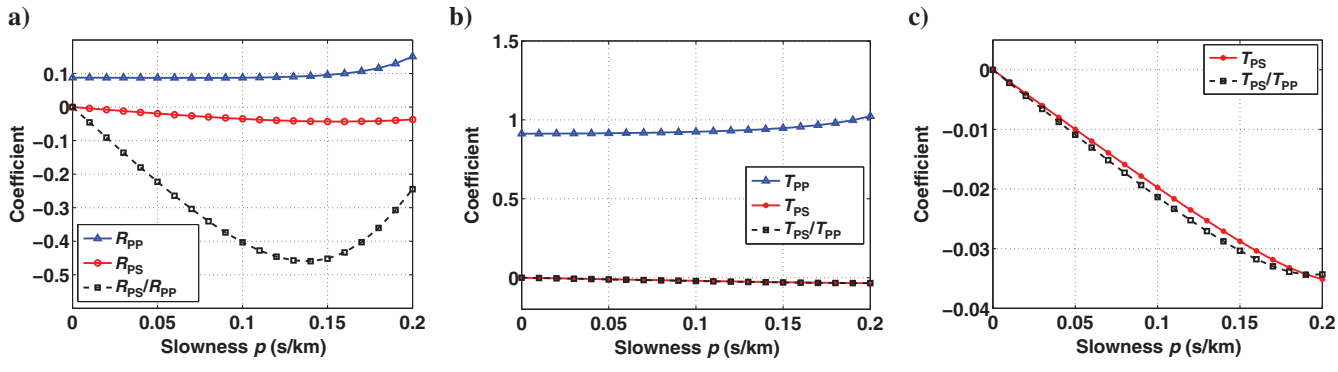

Figure 3. (a) Reflection and reflection-conversion coefficients with their CRCs and (b) transmission and transmission conversion with their CRCs shown for an incident P-wavefield against horizontal slowness, $\mathrm{P} = \sin(\theta)/V_p$ where θ is the P-wave incident angle and $V_P = 4$ km/s, $V_S = 2$ km/s, $\rho = 2$ g/cm^3, and $\Delta V_P = 0.5$ km/s, $\Delta V_S = 0.1$ km/s, and $\Delta\rho = 0.1$ g/cm^3. Panel (c) is a magnification of a portion of panel (b).

Two half-space model

A two half-space model with an interface at 2 km depth was used with values identical to the model used to generate Figure 3. In Figure 5, we show the comparison between the analytical and numerical CRCs in which the numerical CRCs are calculated from amplitude-variation-with-angle (AVA) response extracted from the SICW image at the depth of the interface. Although the AVA response of the SICW image can be calculated using a single source due to the lateral invariance of the two half-space model, we stacked 11 images to mitigate numerical artifacts. The images were stacked such that the zero incident angle and source location on the surface of each image are vertically aligned. In Figure 5a, we show the comparison of CRCs with P-wave illumination deconvolution SICW-IC (equation 9) and in Figure 5b with the normalized deconvolution SICW-IC (equation 14). To remove acquisition effects from the AVA response, we apply a dip filter to remove spurious arrivals. We observe that despite the limited aperture at the small and large slownesses (i.e., angles), the AVA response at intermediate slownesses agrees well, verifying the relationship established above between CRCs and SICW-ICs.

Marmousi model

We use the P-wave speed from the original Marmousi model shown in Figure 6a with constant density of 2500 kg/m^3 and V_P/V_S of two. The number of grid points in the models is $N_z = 150$ and $N_x = 267$ (excluding 20 PML grid points in each direction), and the spatial increments are $\Delta x = \Delta z = 12$ m. In Figure 6b, we show a model of discontinuities for Marmousi that we use as a reference for evaluating the imaging results: This model was produced from the difference between the original squared P-wave slowness (Figure 6a) and a spatially smoothed squared P-wave slowness used in the imaging process. The smoothing is more than two points in both spatial directions. We model two sets of sources using a Ricker source wavelet with a peak frequency of 30 Hz and time step of 0.0005 s. Each set consists of 27 sources with vertical point force mechanism, equally distributed horizontally with 120 m spacing at one of two depths: one at the surface, 0 km, and one at a depth of 1.7 km. The seismic data are recorded for 3 s with two-component receivers that are equally distributed and span the same computational grid at the surface. The reason for choosing source sets at two depths is to test the transmission-like and reflection-like acquisition geometries, and the reason for choosing only 27 sources is to show that SICW images can be obtained with a relatively small number of shots from active source acquisition or passive source monitoring. Although for the former, it is related to an acquisition cost, for the latter, it may be difficult to identify a large number of passive source quakes with good signal quality (i.e., where wave modes are observed), so the ability to form an image with a small number of sources may be crucial for passive source imaging. Note that because no forward source propagation is required to form an SICW image, there should be no image artifacts due to uncertainties in the source location.

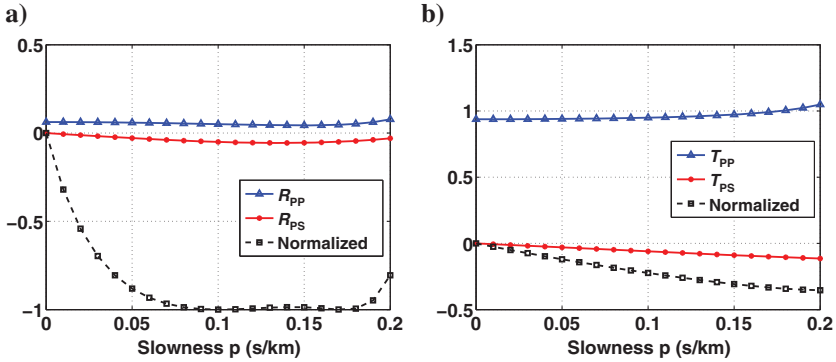

Figure 4. Normalized CRCs (equations 12 and 13) for the two half-space example shown in Figure 3.

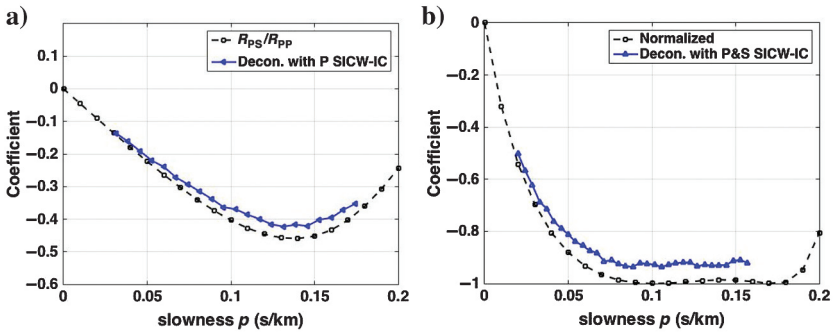

Figure 5. Comparison between the analytical CRCs (equations 6 and 12) and AVA responses from SICW images with (a) deconvolution P-wave illumination (equation 9) and (b) deconvolution P- and S-wave illumination (equation 14). The AVA responses were derived from 11 stacked half-space images in which zero slowness is aligned with source location on the surface.

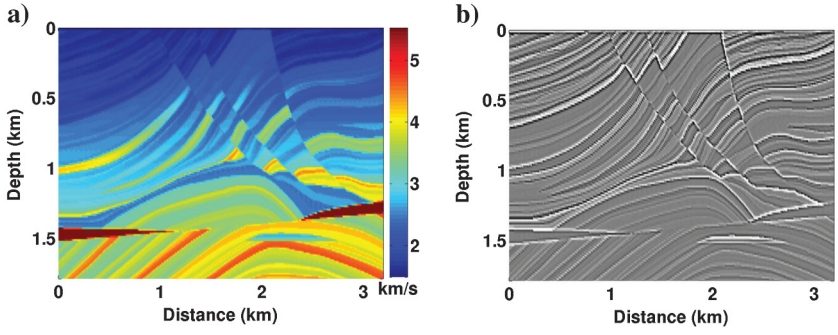

Figure 6. (a) Marmousi P-wave speed model and (b) model of discontinuities produced by taking the difference between the original slowness squared of panel (a) and its smoothed squared model.

In Figure 7, we show the imaging results produced with sources on the surface and the four imaging conditions given in equations 9, 10, 11, and 14. We have applied no vertical gain nor compensation for geometric spreading, in contrast to common practice (e.g., Claerbout, 1985, p. 235), to highlight the differences between different imaging conditions. Figure 7a, obtained with the deconvolutional SICW-IC with P-wave illumination (equation 9), shows good amplitude balancing with depth, although it amplifies the shallow part, particularly at the top right between 0 and 0.4 km in depth and 2 and 3 km in horizontal distance. The result in Figure 7b, obtained with the deconvolutional SICW-IC with S-wave illumination (equation 10), is the most similar to the model of discontinuities (the reference model is shown in Figure 6b) and shows higher resolution because of the short S-wavelengths. However, it suffers from noise, caused by instabilities in the imaging condition. Figure 7c, obtained with equation 11, has amplitudes that are clearly attenuated with

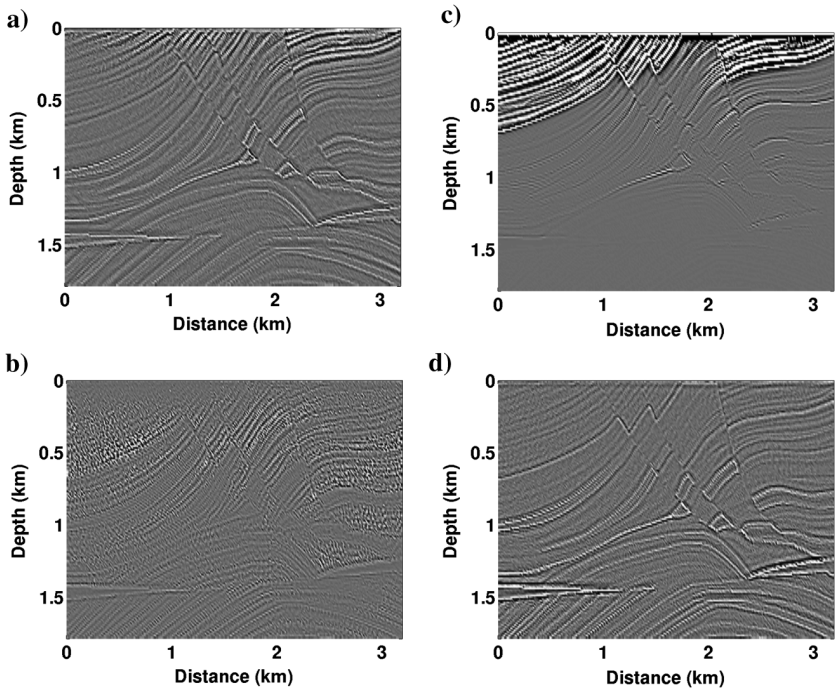

Figure 7. Migrated images produced with 27 sources with 0.12 km horizontal intervals at the surface and receivers at the surface using (a) deconvolutional SICW-IC with P-wave illumination (equation 9), (b) deconvolutional SICW-IC with S-wave illumination (equation 10), (c) crosscorrelational SICW-IC (equation 11), and (d) deconvolutional SICW-IC with normalized illumination (equation 14). The source mechanism of each source is a vertical point force and the V_P/V_S is two. The amplitudes in panels (a and c) are attenuated with depth; in panel (b) the image is noisy, whereas in panel (d), the image amplitudes are most balanced, particularly at the shallow depths between 0 and 0.4 km and in the regions containing anticlines, compared with those in panels (a-c).

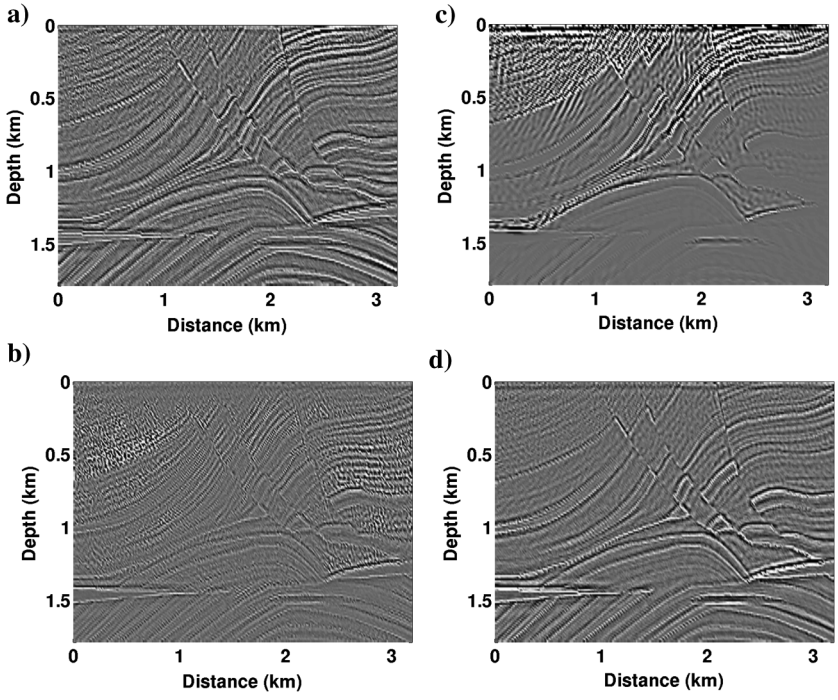

Figure 8. Migrated images produced with 27 sources with 0.12 km horizontal intervals at the depth of 1.7 km and receivers at the surface using (a) deconvolutional SICW-IC with P-wave illumination (equation 9), (b) deconvolutional SICW-IC with S-wave illumination (equation 10), (c) crosscorrelational SICW-IC (equation 11), and (d) deconvolutional SICW-IC with normalized illumination (equation 14). The source mechanism of each source is a vertical point force, and the V_P/V_S is two.

depth. The image in Figure 7d produced by equation 14 is similar to Figure 7a. However, although certain small-scale interface continuities are lost, the amplitudes in Figure 7d are considerably better balanced and have better spatial resolution with depth when using P- and S-illuminating wavefields, compared with those in Figure 7a–7c (see particularly the shallow region between 0 and 0.4 km in depth, and the deep region of anticlines).

In Figure 8, we present images generated with sources at a depth of 1.7 km. We observe again that the image obtained with the crosscorrelational SICW-IC has poorer amplitude recovery compared with those produced with the deconvolutional SICW-ICs. Also the image with the normalized illumination, Figure 8d has amplitudes balanced most similarly to that of the reference model (Figure 6b).

As mentioned above, Figures 7 and 8 were obtained with a small number of 27 sources, in Figure 9, we show SICW images obtained with 130 sources at the surface with 24 m horizontal increment to illustrate how the quality and resolution of each SICW image changes when the number of sources is increased. We observe that noise level decreases in the three deconvolutional SICW images with increased number of sources compared with Figure 7a, 7b, and 7d, but the overall amplitude balancing remains similar. However, the amplitude balancing of the crosscorrelation SICW image has significantly changed compared with Figure 7c. This observation illustrates that with a limited number of sources, the deconvolutional SICW-ICs generate balanced images.

Imaging quality is always dependent on the quality of the wave speed models used for imaging. For this reason, we have developed a wave speed estimation approach for use with SICW imaging that allows one to find reliable wave speed models and thus obtain improved images (Shabelansky et al., 2015b). To highlight the sensitivity of SICW-ICs to wave speed variations, we present two sets of imaging results; first with severely smoothed wave speed models and second with a smooth elliptical inclusion at the center of the S-wave speed model. The smoothing is over 30 points in both spatial directions in both sets. In Figure 10a–10d, we show SICW images with smoothed P-wave speed and correct S-wave speed and density, in which we observe that the smoothed P-wave speed has minor effect on all SICW-ICs. In Figure 10e–10h, the S-wave speed is smoothed and the P-wave speed and density are correct. Now, we observe a significant image degradation obtained with the crosscorrelation, deconvolution with P-wave illumination and with both wave illuminations SICW-ICs. However, the SICW image obtained with S-wave illumination (Figure 10f) interestingly is insensitive to S-wave variation. In Figure 10i–10l, we show the images that are obtained with P- and S-wave speeds smoothed. We observe that because the V_P/V_S ratio is preserved the image degradation is less severe than when only one wave speed is smoothed; however, the noise level is higher than with other cases. In Figure 10m–10p, we show the SICW images obtained with the correct P-wave speed and S-wave speed, which consisted of the correct S-wave speed with an elliptical perturbation at the center of the model. The reason for inserting the elliptical inclusion into the S-wave speed model stems from the observations of Figure 10e–10h in which we observed that SICP images have strong sensitivity to the S-wave speed variations. We observe that the effect of the elliptical inclusion is very pronounced in the deconvolution SICW image with P-wave illumination (Figure 10m) and in the crosscorrelation SICW image (Figure 10o); we observe strong amplitude amplification at the area of the S-wave speed inclusion. In the deconvolution SICW image with both illuminations (Figure 10p), we observe that the amplitudes are attenuated but the image is clear, whereas the SICW image with S-wave illumination (Figure 10n) is insensitive to the inclusion in the S-wave speed model. The insensitivity to S-wave speed is similar to the observation made for Figure 10f.

To show a comparison between the SICW-ICs and the source-dependent ICs, we calculate elastic PP RTM images with crosscorrelation and deconvolution ICs (i.e., we replace the back-propagating S-wavefield in equations 9 and 11 with the forward-propagating P-wavefield, respectively). We use the same number of surface sources, receiver geometry, and the same wave speeds as those calculated above in Figure 7. We apply a mute to remove the direct arrivals in the data. Because the source-dependent RTM produces images of reflections of the subsurface and the SICW-ICs produce images of the ratios between conversions and reflections, the comparison

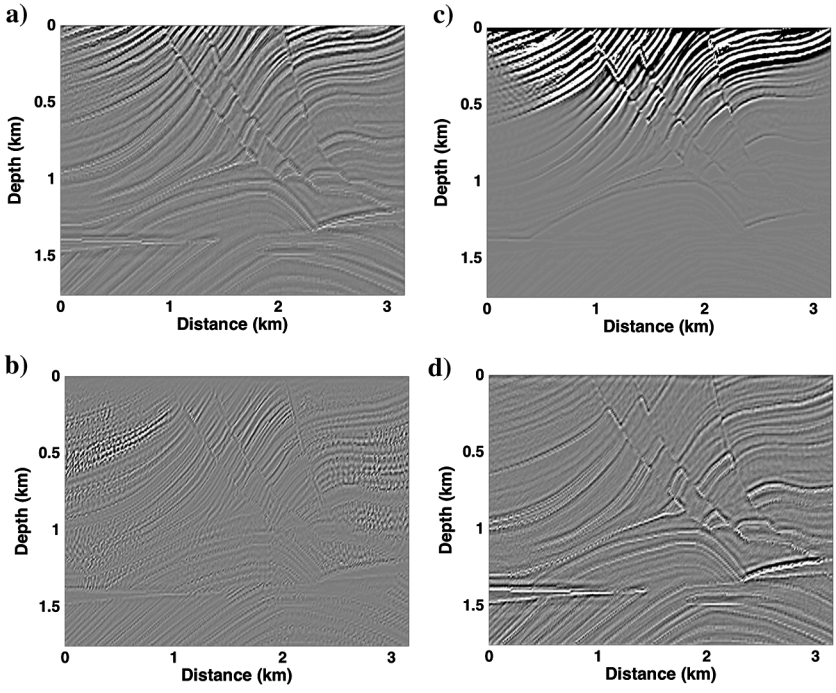

Figure 9. Migrated images produced with 130 sources with 24 m horizontal intervals at the surface and receivers at the surface using (a) deconvolutional SICW-IC with P-wave illumination (equation 9), (b) deconvolutional SICW-IC with S-wave illumination (equation 10), (c) crosscorrelational SICW-IC (equation 11), and (d) deconvolutional SICW-IC with normalized illumination (equation 14). The images are less noisy than those in Figure 7. Although the amplitude balancing of the crosscorrelation SICW image was changed due to the increased number of sources, the amplitude balancing of the deconvolutional SICW images remained the same as in those with a reduced number of sources (Figure 7a, 7b, and 7d).

presented here highlights only the kinematic effects. In Figure 11a, we show the source-dependent elastic crosscorrelational RTM (implicitly given in equation 4), and in Figure 11b, we show the source-dependent elastic deconvolution RTM with source wavefield illumination (implicitly given in equation 3). We observe that similarly to the SICW-ICs, the image obtained with the source-dependent crosscorrelational IC (Figure 11a) has poorer amplitude recovery with depth compared with that produced with the deconvolutional IC (Figure 11b). We also observe that although the deconvolutional IC (Figure 11b) suppresses the effect of the source locations at the shallow portion of the image, both images are noisier at the near surface than the SICW images (see Figure 7 for comparison). Both source-dependent images also have less consistent amplitudes with depth than the deconvolutional SICW images.

Marmousi II

To test the applicability of the four SICW-ICs to models having variable V_P/V_S and density, we use the Marmousi II model. We extract a part of the model around the area used for the Marmousi I model above to reduce the computational cost. In Figure 12, we show the P-, S-, P/S, and S/P impedance contrasts, respectively, as references for evaluating imaging results to highlight interfaces of the images and the subtle differences between the impedances. The P- and S-impedance contrasts are produced from the spatial finite differences of the impedances. For P/S and S/P impedance contrasts, a small number was added to avoid division by zero. The number of computational grid points is $N_z = 618$, $N_x = 1220$ with spatial increments of $dz = dx = 5$ m. We generate 27 vertical-point

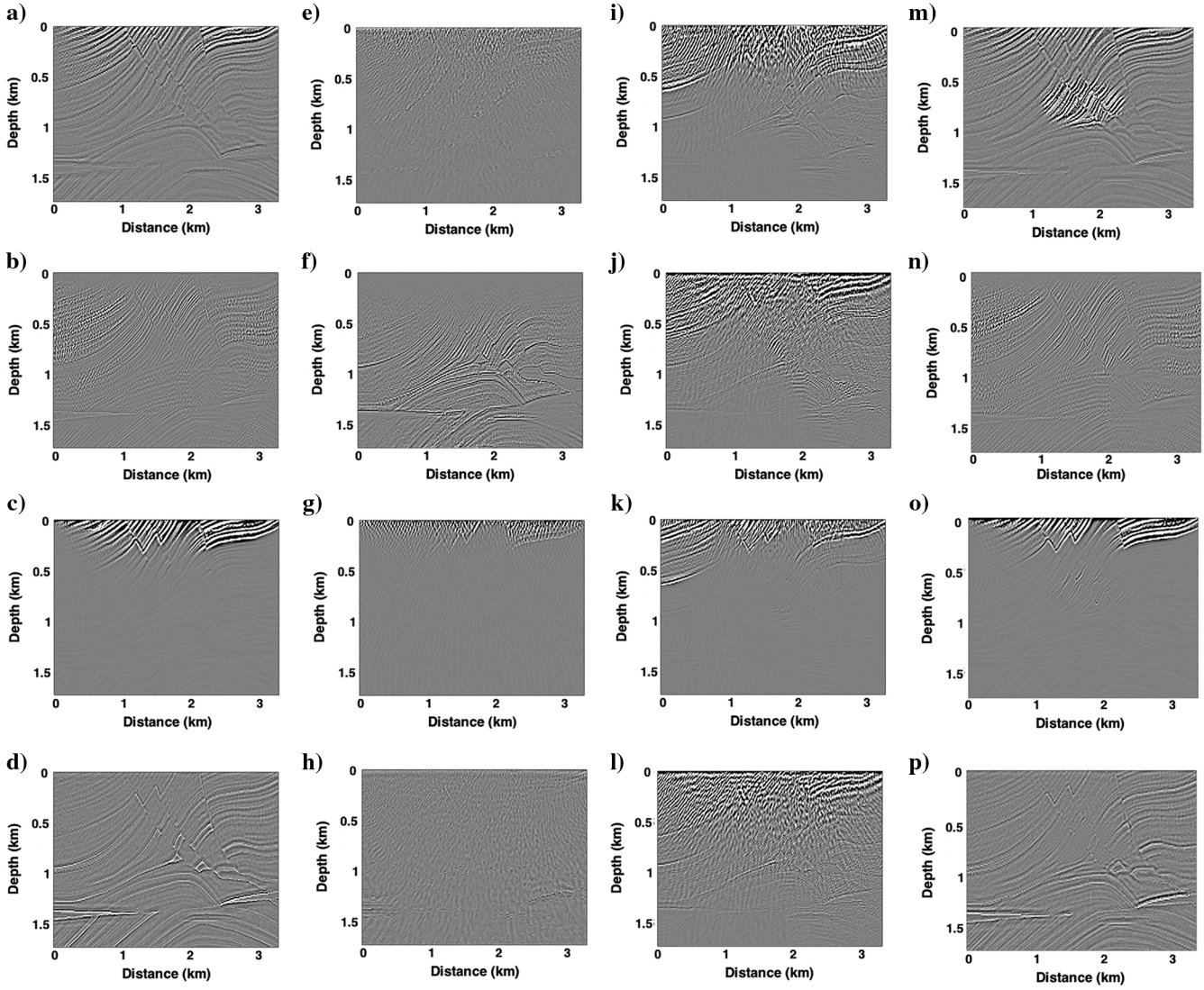

Figure 10. Migrated images produced with sources and receivers at the surface with different elastic wave-speed variations: (first column) only P-wave speed severely smoothed, (second column) only S-wave speed severely smoothed, (third column) P- and S-waves severely smoothed, and (fourth column) elliptical perturbation in S-wave speed, (first row) deconvolutional SICW-IC with P-wave illumination (equation 9), (second row) deconvolutional SICW-IC with S-wave illumination (equation 10), (third row) crosscorrelational SICW-IC (equation 11), and (fourth row) deconvolutional SICW-IC with normalized illumination (equation 14). The smoothing of each wave speed was more than 30 points in both spatial directions. The source mechanism of each source is a vertical point force. Note the images at panels (f and n) are least sensitive to S-wave speed variations.

force sources on the surface with a horizontal increment of 0.2 km and recorded them with two-component receivers on the surface for 2.4 s with time step of 0.0002 s. We use a Ricker source wavelet with a peak frequency of 10 Hz. In Figure 13, we show SICW imaging results obtained with the deconvolution P-wave illumination, deconvolution S-wave illumination, crosscorrelation, and deconvolution with P- and S-waves illumination, respectively. As with the Marmousi I model, we observe that the deconvolution SICW-ICs produce better balanced images than those obtained with the crosscorrelation SICW-IC. Also the deconvolution SICW image obtained with P- and S-wave illumination (Figure 13d) has a better similarity with the P/S and S/P impedance contrasts (Figure 12c and 12d) and produces a better amplitude balanced image than that with either P- or S-wave illumination. The results with the Marmousi II model show that the SICW-ICs are robust with respect to variable V_P/V_S and density models. The result for the crosscorrelation SICW-IC with variable density only is presented by Shabelansky et al. (2014).

DISCUSSION

In the examples and results presented above, we illustrated the properties and applicability of SICW-ICs to understand what is imaged with each SICW-IC and how to produce more balanced SICW images. We investigated the robustness of the four SICW imaging conditions with simple and complicated synthetic models and showed that each SICW-IC gives different image amplitudes. There are still several remaining questions, however. In this section, we will address four of the most pressing.

The first question is how to choose the stabilization factor ϵ for the deconvolutional amplitude-balancing ICs, given in equations 9, 10, and 14. This factor controls the stability and quality of the imaging process (i.e., ensuring that division by zero is not taking place) and is different for different ICs and data sets. To our knowledge, there is no good strategy to estimate this parameter before an image has been constructed. Although we found that by setting the value of ϵ to be between 5% and 10% of the maximum amplitude of the crosscorrelation SICW image made with a single source would stabilize the deconvolutional SICW-IC, an approach from Marquardt (1963) may improve the robustness of the procedure for estimating an appropriate stabilization factor. However, it might make the run time of SICW imaging significantly more expensive. The stabilization factor may also be spatially variable as a function of a wave speed or density. This is a subject for future research.

The second question is how sensitive the SICW-ICs are to uncertainties in P- and S-wave speeds, and how these uncertainties can be mitigated. The sensitivity of the four SICW-ICs to variations in both wave speeds can be high, and the image can be completely degraded in some cases as shown in Figure 10. However, we found that the deconvolutional SICW-IC with S-wave illumination is less sensitive to S-wave uncertainty than the other three SICW-ICs, and when the V_P/V_S is preserved, the image degradation is less severe (Figure 10f). Shabelansky et al. (2015b) present an approach based on the SICW-IC for P- and S-wave speed reconstruction. This method is based on the crosscorrelational form; wave-speed updating based on the deconvolutional forms is a subject of future research.

The third question is how to relate the produced SICW images to physical parameters. The deconvolutional SICW imaging conditions were derived above from the CRCs, which could be a stand-alone physical quantity and may be treated as complementary to reflection, transmission, and conversion coefficients. Thus, the

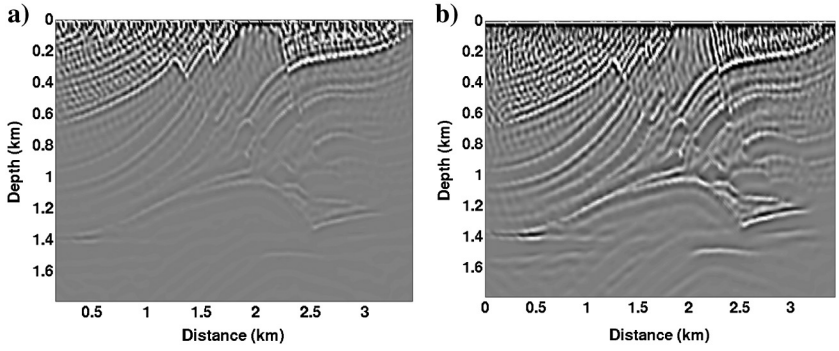

Figure 11. Source-dependent elastic RTM images produced with the same 27 surface sources and receivers as those shown in Figure 7 using (a) crosscorrelational and (b) deconvolutional imaging conditions between P-source and P-receiver wavefields. Note how the small number of sources degrades the quality of the image near the shallow subsurface.

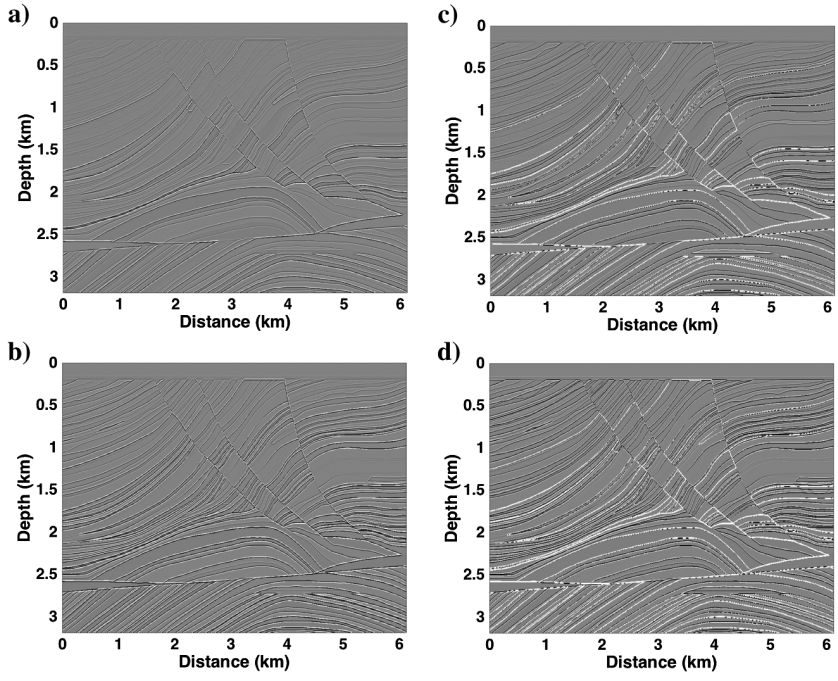

Figure 12. Marmousi II model for a similar area as used for the Marmousi I model shown in Figure 6: (a) P-wave impedance contrast, (b) S-wave impedance contrast, (c) P-/S-wave impedance contrast, and (d) S-/P-wave impedance contrast.

images could be associated by inversion with the CRCs. In particular, the CRCs may be of great interest in studies of amplitude variation with offset/angle/azimuth because they define the ratio of the converted and pure seismic waves and how their energy is partitioned after passing through an impedance contrast.

The fourth question is how to apply SICW imaging to an anisotropic medium using the four imaging conditions. The success of SICW imaging in an anisotropic medium depends on the ability to separate the propagating waves into quasi P- and S-waves. For VTI media, many studies show different techniques for wave separation (Dellinger and Etgen, 1990; Yan and Sava, 2009; Yan, 2010; Zhang and McMechan, 2010; Cheng and Fomel, 2014). However, they are significantly more computationally expensive than that shown in Appendix A for the isotropic case. For a more general anisotropy, even further research is required, particularly in 3D.

Our approach relies on wavefield separation using the method described in Appendix A, and it does not require knowledge of the normal vector from subsurface reflectors as in Duan and Sava (2015), an estimation of the wavefield vector propagation directions as in Gong et al. (2016), or an estimation of the Poynting vectors as in Wang and McMechan (2015). The general observations and discussions drawn throughout the text in 2D are expected to be similar in 3D. The application of the 3D crosscorrelational SICW-IC to field data can be found in Shabelansky (2015, chapter 5). We have introduced a novel approach for source-independent seismic imaging and illustrated it with a limited number of numerical examples that are meant to highlight the differences among the proposed imaging conditions. We hope that others will explore more numerical examples to evaluate the SICW-ICs and apply them to field data.

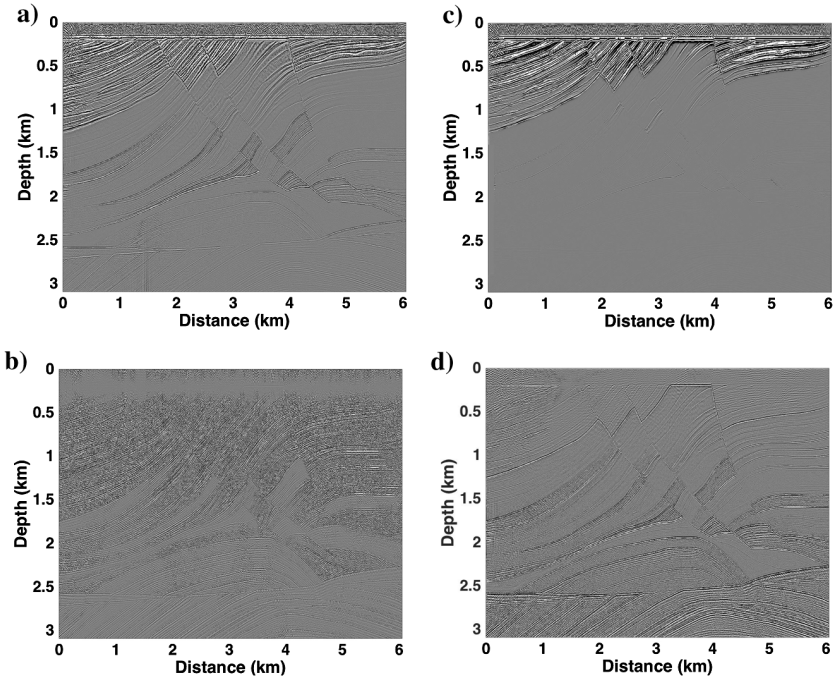

Figure 13. Marmousi II: migrated images produced with 27 sources with 0.2 km horizontal interval at the surface and receivers at the surface using (a) deconvolutional SICW-IC with P-wave illumination (equation 9), (b) deconvolutional SICW-IC with S-wave illumination (equation 10), (c) crosscorrelational SICW-IC (equation 11), and (d) deconvolutional SICW-IC with normalized illumination (equation 14). The source mechanism of each source is a vertical point force. Despite a certain level of noise in all images, the image amplitudes in panel (d) are the most balanced.

CONCLUSION

We have presented crosscorrelational and deconvolutional forms of an SICW-IC, and we investigated their relationship with reflection, transmission, and conversion coefficients through a newly introduced concept of CRCs. We illustrated the properties of the CRCs and demonstrated their use through deconvolutional imaging conditions with different types of illumination compensation. We tested the imaging conditions with a two half-space model, and the synthetic Marmousi I and II models. We also showed the sensitivity of the SICW-ICs to P- and S-wave speed perturbations and presented a comparison between the SICW-ICs and the source-dependent elastic RTM. The results show advantages when appropriate illumination compensation in SICW-IC is applied and that SICW-IC with S-wave illumination is less sensitive to S-wave speed perturbation than the other SICW-ICs. The introduced SICW-ICs present attractive alternatives to elastic source-dependent RTM imaging.

ACKNOWLEDGMENTS

We thank ConocoPhillips and the Earth Resources Laboratory (ERL) founding members consortium at MIT for funding this work. Partial support for this work was provided by the Department of Energy, Lawrence Berkeley National Laboratory, subcontract #6927716, entitled, "Advanced 3D Geophysical Imaging Technologies for Geothermal Resource Characterization." We acknowledge S. K. Bakku, A. Tryggvason, and O. Gudmundsson for their helpful discussions. We also acknowledge the associate and assistant editors and six anonymous reviewers whose comments helped significantly to improve the manuscript.

APPENDIX A

P-S WAVEFIELD SEPARATION USING ACCELERATION DECOMPOSITION

The images produced with P- and S-waves depend on the P-S wavefield separation. Separation using the Helmholtz decomposition (i.e., applying only the divergence and curl operators) produces images with inconsistent amplitude and phase that thus require correction before or after the construction of the images (Sun et al., 2004, 2011; Shang et al., 2012; Shabelansky et al., 2013b). Separation using the vector wavefield decomposition is computationally more expensive, but it produces images with consistent amplitude polarity.

The vector wavefield separation is derived from the isotropic elastic-wave equation for a smooth medium (Aki and Richards, 2002, p. 64) as

$$\ddot{\mathbf{u}} = \alpha^2 \nabla\nabla \cdot \mathbf{u} - \beta^2 \nabla \times \nabla \times \mathbf{u}, \qquad \text{(A-1)}$$

where $\mathbf{u}(\mathbf{x}, t)$ and $\ddot{\mathbf{u}}(\mathbf{x}, t)$ are the displacement and acceleration vector wavefields, $\alpha(\mathbf{x})$ and $\beta(\mathbf{x})$ are

the P- and S-wave speeds, and ∇, $\nabla\cdot$, and $\nabla\times$ are the gradient, divergence, and curl operators, respectively. Because the acceleration wavefield is decomposed into $\alpha^2\nabla\nabla\cdot\mathbf{u}$ and $-\beta^2\nabla\times\nabla\times\mathbf{u}$, we define $\ddot{\mathbf{u}}=\ddot{\mathbf{u}}_P+\ddot{\mathbf{u}}_S$ with

$$\ddot{\mathbf{u}}_P(\mathbf{x},t)=\alpha^2(\mathbf{x})\nabla\nabla\cdot\mathbf{u}(\mathbf{x},t),$$
$$\ddot{\mathbf{u}}_S(\mathbf{x},t)=-\beta^2(\mathbf{x})\nabla\times\nabla\times\mathbf{u}(\mathbf{x},t), \quad \text{(A-2)}$$

where $\ddot{\mathbf{u}}_P$ and $\ddot{\mathbf{u}}_S$ are the P- and S-components of acceleration. Because $\alpha(\mathbf{x})$ and $\beta(\mathbf{x})$ are in general smooth for imaging, we remove the effect of the P- and S-wave speeds on wavefield separation and obtain

$$\mathbf{u}_P=\nabla\nabla\cdot\mathbf{u}, \qquad \mathbf{u}_S=-\nabla\times\nabla\times\mathbf{u}, \quad \text{(A-3)}$$

where $\mathbf{u}_P(\mathbf{x},t)$ and $\mathbf{u}_S(\mathbf{x},t)$ are the P- and S-vector components of the separated displacement vector wavefield $\mathbf{u}(\mathbf{x},t)$ with the velocities removed in equation A-2. By removing the (squared) wave speeds from equation A-2, we obtain units of inverse displacement (i.e., $1/\text{m}$) in equation A-3. Note that the operators $\nabla\nabla\cdot$ and $-\nabla\times\nabla$ in equation A-2 can be similarly applied to the particle velocity or acceleration wavefields. Then the units of the separated wavefields will be proportional to $1/\text{ms}$ or $1/\text{ms}^2$, respectively. The wave speed removal procedure reduces strong dependence of imaging on wave speeds and thus produces more balanced images. However, for wave speed optimization analysis, care needs to be taken because this procedure affects to construction of the gradient for the optimization. For more details, see Shabelansky et al. (2015b) and Shabelansky (2015, appendix B).

REFERENCES

Aki, K., and P. G. Richards, 2002, Quantitative seismology, theory and methods, 2nd ed.: University Science Books.

Baysal, E., D. D. Kosloff, and J. W. C. Sherwood, 1983, Reverse time migration: Geophysics, **48**, 1514–1524, doi: 10.1190/1.1441434.

Bleistein, N., 1987, On the imaging of reflectors in the earth: Geophysics, **52**, 931–942, doi: 10.1190/1.1442363.

Brytic, V., M. V. de Hoop, and R. D. van der Hilst, 2012, Elastic-wave inverse scattering based on reverse time migration with active and passive source reflection data, *in* G. Uhlmann, ed., Inverse problems and applications: Inside out II: MSRI Publications 60, 411.

Chang, W.-F., and G. A. McMechan, 1994, 3-D elastic prestack, reverse-time depth migration: Geophysics, **59**, 597–609, doi: 10.1190/1.1443620.

Chattopadhyay, S., and G. A. McMechan, 2008, Imaging conditions for prestack reverse time migration: Geophysics, **73**, no. 3, S81–S89, doi: 10.1190/1.2903822.

Cheng, J., and S. Fomel, 2014, Fast algorithms for elastic-wave-mode separation and vector decomposition using low-rank approximation for anisotropic media: Geophysics, **79**, no. 4, C97–C110, doi: 10.1190/geo2014-0032.1.

Claerbout, J. F., 1971, Toward a unified theory of reflector mapping: Geophysics, **36**, 467–481, doi: 10.1190/1.1440185.

Claerbout, J. F., 1985, Imaging the earth's interior: Blackwell Scientific Inc.

Dellinger, J., and J. Etgen, 1990, Wave-field separation in two-dimensional anisotropic media: Geophysics, **55**, 914–919, doi: 10.1190/1.1442906.

Duan, Y., and P. Sava, 2015, Scalar imaging condition for elastic reverse time migration: Geophysics, **80**, no. 4, S127–S136, doi: 10.1190/geo2014-0453.1.

Gong, T., B. D. Nguyen, and G. A. McMechan, 2016, Polarized wavefield magnitudes with optical flow for elastic angle-domain common-image gathers: Geophysics, **81**, no. 4, S239–S251, doi: 10.1190/geo2015-0518.1.

Kaelin, B., and A. Guitton, 2006, Imaging condition for reverse time migration: 76th Annual International Meeting, SEG, Expanded Abstracts, 2594–2598.

Marquardt, D. W., 1963, An algorithm for least-squares estimation of nonlinear parameters: Journal of the Society for Industrial & Applied Mathematics, **11**, 431–441, doi: 10.1137/0111030.

Nihei, K. T., S. Nakagawa, and L. R. Myer, 2001, Fracture imaging with converted elastic waves: Lawrence Berkeley National Laboratory, LBNL–50789.

Popovici, A. M., 1996, Prestack migration by split-step DSR: Geophysics, **61**, 1412–1416, doi: 10.1190/1.1444065.

Schneider, W. A., 1978, Integral formulation for migration in two and three dimensions: Geophysics, **43**, 49–76, doi: 10.1190/1.1440828.

Schleicher, J., J. C. Costa, and A. Novais, 2008, A comparison of imaging conditions for wave-equation shot-profile migration: Geophysics, **73**, no. 6, S219–S227, doi: 10.1190/1.2976776.

Shabelansky, A. H., 2015, Theory and application of source independent full wavefield elastic converted phase seismic imaging and velocity analysis: Ph.D. thesis, Massachusetts Institute of Technology.

Shabelansky, A. H., M. C. Fehler, and A. E. Malcolm, 2013a, Converted-phase seismic imaging of the Hengill region, southwest Iceland: Presented at the AGU Fall Meeting Abstracts, A2461.

Shabelansky, A. H., A. Malcolm, and M. Fehler, 2015a, Converted-phase seismic imaging-amplitude-balancing source-independent imaging conditions: 77th Annual International Conference and Exhibition, EAGE, Extended Abstracts, doi: 10.3997/2214-4609.201412937.

Shabelansky, A. H., A. Malcolm, M. Fehler, and W. L. Rodi, 2014, Migration-based seismic trace interpolation of sparse converted phase micro-seismic data: 84th Annual International Meeting, SEG, Expanded Abstracts, 3642–3647.

Shabelansky, A. H., A. Malcolm, M. Fehler, X. Shang, and W. L. Rodi, 2013b, Converted phase elastic migration velocity analysis: 83rd Annual International Meeting, SEG, Expanded Abstracts, 4732–4737.

Shabelansky, A. H., A. Malcolm, M. C. Fehler, X. Shang, and W. L. Rodi, 2015b, Source-independent full wavefield converted-phase elastic migration velocity analysis: Geophysical Journal International, **200**, 952–966, doi: 10.1093/gji/ggu450.

Shang, X., M. de Hoop, and R. van der Hilst, 2012, Beyond receiver functions: Passive source reverse time migration and inverse scattering of converted waves: Geophysical Research Letters, **39**, 1–7, doi: 10.1029/2012GL052289.

Stoffa, P. L., J. T. Fokkema, R. M. de Luna Freire, and W. P. Kessinger, 1990, Split-step Fourier migration: Geophysics, **55**, 410–421, doi: 10.1190/1.1442850.

Sun, R., G. A. McMechan, and H.-H. Chuang, 2011, Amplitude balancing in separating P- and S-waves in 2D and 3D elastic seismic data: Geophysics, **76**, no. 3, S103–S113, doi: 10.1190/1.3555529.

Sun, R., G. A. McMechan, H.-H. Hsiao, and J. Chow, 2004, Separating P-and S-waves in prestack 3D elastic seismograms using divergence and curl: Geophysics, **69**, 286–297, doi: 10.1190/1.1649396.

Valenciano, A., and B. Biondi, 2003, 2-D deconvolution imaging condition for shot-profile migration: 73rd Annual International Meeting, SEG, Expanded Abstracts, 1059–1062.

Wang, W., and G. A. McMechan, 2015, Vector-based elastic reverse time migration: Geophysics, **80**, no. 6, S245–S258, doi: 10.1190/geo2014-0620.1.

Xiao, X., and W. S. Leaney, 2010, Local vertical seismic profiling (VSP) elastic reverse-time migration and migration resolution: Salt-flank imaging with transmitted P-to-S waves: Geophysics, **75**, no. 2, S35–S49, doi: 10.1190/1.3309460.

Yan, J., 2010, Wave-mode separation for elastic imaging in transversely isotropic media: Ph.D. thesis, Colorado School of Mines.

Yan, J., and P. Sava, 2009, Elastic wave-mode separation for VTI media: Geophysics, **74**, no. 5, WB19–WB32, doi: 10.1190/1.3184014.

Youn, O. K., and H.-W. Zhou, 2001, Depth imaging with multiples: Geophysics, **66**, 246–255, doi: 10.1190/1.1444901.

Zhang, Q., and G. A. McMechan, 2010, 2D and 3D elastic wavefield vector decomposition in the wavenumber domain for VTI media: Geophysics, **75**, no. 3, D13–D26, doi: 10.1190/1.3431045.

Zhang, Y., and J. Sun, 2008, Practical issues of reverse time migration-true-amplitude gathers, noise removal and harmonic-source encoding: 70th Annual International Conference and Exhibition, EAGE, Extended Abstracts, doi: 10.3997/2214-4609.20147708.